Evidence of kilometer-wide shallow bulk plastic yielding along the 2021 Maduo, Tibet, surface rupture, and its relation with the dynamic rupture process

S. L. Antoine[1,2], Z. Liu[1], A. Delorme[2], Y. Klinger[2]

[1] NASA Jet Propulsion Laboratory, California Institute of Technology, Pasadena, California, USA

[2] Université de Paris Cité, Institut de physique du globe de Paris, CNRS, Paris, France,

Corresponding author: Solène L. Antoine (solene.antoine@jpl.nasa.gov)

Key points:

- The 2021 Maduo earthquake is dominantly associated with kilometer-scale surface diffuse bulk plastic yielding.
- Diffuse bulk plastic yielding occurs in regions where the dynamic stresses could not overcome the shallow fault zone frictional strength.
- This study documents a gradual surface deformation localization along the rupture strike as a function of coseismic displacement.

Abstract

Surface deformation associated with continental earthquake ruptures includes localized deformation on the faults, as well as deformation in the surrounding medium though distributed and/or diffuse processes. However, the connection of the diffuse part of the surface deformation to the overall rupture process, as well as its underlying physical mechanisms are not yet well

understood. Computing high-resolution optical image correlations for the 2021/05/21 M_w7.4 Maduo, Tibet, rupture, we highlight a correlation between the presence of faults and fractures at the surface, and variations in the across-fault displacement gradient, fault zone width, and amplitude of surface displacement. We show that surface slip along primary faults is systematically associated with gradients greater than 1%, and is dominant in regions of greater coseismic surface displacement. Conversely, the diffuse deformation is associated with gradients ≤0.3%, and is dominant in regions of lesser surface displacement. The distributed deformation then occurs for intermediate gradients of 0.3-1%, and at the transition between the localized and diffuse deformation regions. Such patterns of deformation are also described in laboratory experiments of rock deformation, themself supported by field observations. Comparing these experiments to our observations, we demonstrate that the diffuse deformation along the 2021 Maduo rupture corresponds to kilometer-wide plastic yielding of the bulk medium occurring in regions where surface rupture is generally missing. Along the 2021 Maduo rupture, diffuse deformation occurs primarily in the epicentral region, where the dynamic stresses associated with the nascent pulse-like rupture could not overcome the shallow fault zone frictional strength.

Plain Language

Surface deformation associated with major continental earthquakes generally occurs along faults which are visible at the surface. However, in the case of the 2021 Mw7.4 Maduo, Tibet, rupture, the surface rupture exhibits a discounted trace with kilometer-long gaps, and a primarily diffuse surface deformation, raising the following question: What processes can explain the primarily diffuse deformation along the 2021 Maduo surface rupture? Calculating high-resolution (0.5 m) displacement maps along the 2021 Maduo rupture area, we highlight that the diffuse deformation

gradients, which can have a kilometer-wide extension across the fault zone, accommodate up to 1.5 m of ground surface displacement in regions where the faults did not rupture. Deriving evolution laws for the different deformation components, we highlight a gradual increase of the displacement localization along the faults with increasing total surface displacement. We then suggest that the diffuse deformation corresponds to diffuse plastic deformation of the rock medium in regions of lesser earthquake displacement, where the faults could not rupture totally throughout the surface. Such diffuse behavior is found primarily in the epicentral area, where the earthquake displacement and associated stresses are lower due to the smaller size of the nascent rupture patch.

Keywords

High-resolution optical image correlation, Maduo, surface displacement, localized, diffuse, distributed deformation, frictional strength, dynamic rupture process

1. Introduction

Fault zones are usually described as confined and layered structures composed of series of primary faults where the majority of the co-seismic deformation occurs, and surrounded by a fractured medium also referred to as the damage zone hosting distributed deformation (Mitchell and Faulkner, 2009; Torabi et al., 2019). However, geodetic (Antoine et al., 2021, 2022; Fialko et al., 2005; Hearn and Fialko, 2009; C. Li et al., 2022; Materna and Bürgmann, 2016), field (Petersen et al., 2011; Rodriguez Padilla and Oskin, 2023), and seismic observations (e.g., Alongi et al., 2022; Perrin et al., 2021; Qiu et al., 2021; Vidale and Li, 2003; Yang, 2015; Yang et al., 2011; Zhou et al., 2022) also showed the existence of a third deformation region, at the

transition between the damage zone and the surrounding intact medium, where diffuse plastic yielding of the rocks would occur. This deformation region is referred to as the diffuse deformation zone (Antoine et al., 2021, 2022). Consequently, the total earthquake surface deformation expresses as a combination of localized deformation on the primary faults, distributed deformation on the secondary fractures, and diffuse deformation in the surrounding medium. Each of these deformation components occurs at a different spatial scale, and together they outline the area where the inelastic permanent deformation takes place (e.g., Barnhart et al., 2020; Rodriguez Padilla et al., 2022; Scott et al., 2018) which we refer to as the Fault Zone (FZ) in this study.

On one hand, the localized deformation corresponds to the surface slip that occurs on the well-defined faults, and usually affects a region of a few meters to a few tens of meters wide. Such localized deformation has been characterized along numerous surface ruptures by mapping the faults, and measuring displacement offsets across anthropic and geomorphic features (e.g., Klinger et al., 2005; Rockwell et al., 2002; Teran, 2015). On the other hand, the distributed and diffuse components of the deformation, together, constitute what is called the off-fault deformation (OFD). OFD affects regions hundreds of meters to a few kilometers away from the primary faults (e.g., Antoine et al., 2021, 2022; Milliner et al., 2016; Mitchell and Faulkner, 2009; Rodriguez Padilla et al., 2022). Within the OFD, the distributed deformation, as defined in this study, corresponds to deformation occurring on series of secondary fractures located away from the main rupture (see also Nurminen et al., 2022; Simone et al., 2022). Because the fractures are visible at the surface, the distributed deformation can be detected in the field or using optical and/or topography data (e.g., Choi et al., 2018; Gold et al., 2015; Simone et al.,

2022). The diffuse deformation, however, is not directly associated with visible fractures and generates continuous kilometer-scale gradients of ground surface displacement which can only be detected using dense geodetic measurements with wide across-fault apertures (Antoine et al., 2021; Antoine et al., 2022; Fialko et al., 2005; Li et al., 2022). Consequently, diffuse deformation is often not reported and included in earthquake displacement budgets, and its role in the rupture process is ignored.

As an inelastic process, though, the diffuse deformation should also affect the mechanical properties of the crustal medium as it is described for the more densely fractured damage zone (Budiansky and O'connell, 1976; Heap et al., 2010; Laws et al., 2003; Yamamoto et al., 2002). Accumulation of such wide inelastic deformation over time would then lead to a compliant behavior of the FZ at wider scale than usually considered (Fialko et al., 2002; Hearn and Fialko, 2009; Materna and Bürgmann, 2016; Rodriguez Padilla and Oskin, 2023). These modifications in the FZ mechanical behavior have an impact on the rupture process, at the scale of an individual earthquake rupture (Barbot et al., 2008; Gombert et al., 2018; Okubo, 2019; Sammis et al., 2009; Zhao et al., 2023), as well over several seismic cycles (Faulkner et al., 2006; Lyakhovsky and Ben-Zion, 2008; Passelègue et al., 2018). Hence, it is critical to improve the characterization of the diffuse deformation, and understand the underlying physical processes and its role in the rupture process and FZ development.

Here, we use high-resolution optical image correlation (OIC) to measure the surface horizontal displacement field associated with the 2021 Maduo earthquake rupture. Horizontal displacement maps allow analyzing the along-strike evolution of the surface displacement and deformation

patterns, including the contribution of each deformation component along with the total surface displacement, the width of the deformation zone (also called fault zone width, FZW), and the tectonic and co-seismic rupture settings. Comparing the OIC measurements with published observations from field and laboratory experiments, this study first aims at demonstrating the permanent and inelastic nature of the diffuse deformation, and then proposing plausible physical underlying mechanisms.

2. The 2021 M_w7.4 Maduo, Tibet, rupture

The 2021 Maduo earthquake rupture occurred along the left-lateral strike-slip Jiangcuo fault, within the Bayan Har block of the Eastern Tibetan plateau, at about 100 km South of the Kunlun fault (Ha et al., 2022; Ren et al., 2022). The geometry and slip rate of the Jiangcuo fault are poorly known. However, paleoseismic studies suggest a slip rate of 0.35-0.55 mm/yr (Pan et al., 2022; Ren et al., 2022). Analysis of geomorphic offsets showed a possible cumulative fault displacement of ~4-5 km, decreasing towards the SE side of the fault (Li et al., 2022). On May 21, 2021 a rupture nucleated at a depth of ~10-17 km, and propagated bilaterally for a total rupture length of ~160 km (Fan et al., 2022; He et al., 2021; Liu et al., 2022; Wei et al., 2022). Published earthquake rupture models suggest a maximum slip of ~5-6 m located at ~3-5 km depth, dominated by mostly left-lateral displacement (e.g., He et al., 2021; Jin and Fialko, 2021; Wei et al., 2022; Xiong et al., 2022). Despite its magnitude, the localized surface rupture associated with the 2021 Maduo event is very discontinuous, and surface deformation occurred for a large part on distributed fractures (Liu et al., 2023; Pan et al., 2022; Ren et al., 2022, 2021; Xie et al., 2022; Yuan et al., 2022). Continuous surface ruptures are primarily reported along the NW and SE extremities of the rupture, while they are separated by two major rupture gaps in the

central part. Field studies reported both left-lateral and vertical offsets with respective maximum amplitudes of 2.6-2.9 m and 0.95-1.8 m (Pan et al., 2022; Ren et al., 2022, 2021; Xie et al., 2022; Yuan et al., 2022). The horizontal component, however, is dominant in the surface deformation, and most horizontal offsets range between 0.5-1.5 m. On average, along the 160-km rupture, the average left-lateral surface displacement from field observations is 0.4 m (Yuan et al., 2022), whereas geodetic studies report average values of ~2-3 m (Jin and Fialko, 2021; Li et al., 2022). This difference is interpreted as a result of large OFD along the Maduo rupture (Li et al., 2022), which corresponds to the distributed and diffuse deformations occurring off the primary faults. Overall, the Maduo earthquake presents an heterogeneous surface deformation, with along-strike transitions from regions where localized deformation is dominant, located along mapped faults, to regions where OFD is dominant. In this regard, the 2021 Maduo rupture constitutes a unique case example for analyzing the patterns of localized, the distributed, and the diffuse deformations, their spatial interactions, as well as the underlying physical mechanisms.

3. Material and Methods

We use high-resolution OIC to capture the near-fault surface displacement associated with the 2021 Maduo rupture. Data include high-resolution stereo and tri-stereo pre-earthquake SPOT6-7 (1.6 m ground sampling distance, gsd) and post-earthquake Pleiades (0.5 m gsd) satellite optical images. In total, fourteen combinations of pre- and post-earthquake images were used to cover the 160 km-long study area from East to West (Fig. S1). All data are downloaded on a High-Performance Computer, and processed using the MicMac correlation photogrammetry and OIC software (Rosu et al., 2015; Rupnik et al., 2017), along with Python, MATLAB, and GDAL for the pre- and post-processing. Pleiades data cover only a ±5 km-wide swath along the 2021

Maduo rupture trace (Figs. 1a,b and S1) thus the calculations are performed only within this area. Even though SPOT6/7 pre-earthquake images have a 1.6 m gsd, all processing steps are performed at a 0.5 m gsd which is the native gsd of the Pleiades images. Impact of the resampling and choice of the common gsd (between 0.5 and 1.6 m) have been tested, and the 0.5 m-gsd results are showing smaller variability and average noise level (Fig. S2).

For each sub-area of the rupture, covered by different high-resolution image pools, (tri-)stereo images from both the pre- and post-earthquake periods are used to calculate, respectively, pre- and post-earthquake Digital Surface Models (DSM). The DSMs are used to orthorectify (correction from viewing angle and topography distortions, and projection in a common ground reference; Leprince et al., 2007; Rupnik et al., 2016) the pre- and post-earthquake optical images, respectively. By using DSMs directly computed from the same images later used for OIC, one reduces possible orthorectification bias due to the use of low-resolution topography models, and georeferencing errors. In addition, the use of distinct pre- and post-earthquake DSMs to orthorectify images acquired before and after the earthquake allows avoiding any error related to change in the topography due to the earthquake. Pairs of pre- and post-earthquake orthorectified images are then cropped to their common areas to perform the OIC. OIC is performed using a correlation window of 2.5 m (5 pixels), a search window of 5-7 m, a sub-pixel correlation step of $1/20^{th}$ of pixel, and a regularization term of 0.3. Taking advantage of the fact that we could use two to three images both for the pre- and post-earthquake periods, we performed OIC for all the possible pairs straddling the earthquake date, and stacked the best results. Stacking operation is performed using a weighted average method based on the correlation score maps output of the OIC process (Delorme et al., 2020). Each pixel is weighted using its correlation score (0-1),

allowing for an increase of the signal to noise ratio. The final stacked OIC results obtained for different sub-areas are corrected for ramp artifacts (bundle block adjustment residual) using lower-resolution SAR-derived horizontal displacement maps from Liu et al. (2022) that provide a common reference. A polynomial function is modeled to the difference between SAR and OIC at low frequency, and removed from the OIC results (Fig. S3a-e). Sentinel-2B OIC was also performed to cross-check the quality of the ramp corrections, and validate our method of ramp removal using SAR results (Figs. S3f and S4). Overall, this method preserves the high-frequency signal, that corresponds to the FZ deformation, along with some other local artefacts (decorrelation in regions with clouds, or affected by large sedimentary transport such as drainages, wetlands and dune fields; Fig. 1a). Through specific shape and/or direct visual identification on optical images, we identified local artefacts and ignored them when performing the analysis of the earthquake-related displacements.

Finally, we tested the possibility of measuring the vertical displacements from the difference in elevation between the post-earthquake and the pre-earthquake DSMs, whose features have been horizontally realigned using the measured horizontal displacement (Antoine et al., 2021, 2022; Delorme et al., 2020). However, except for one area (Fig. S5), the noise level reaches an amplitude ±1 m, which prevents any systematic analysis of the vertical deformation. Thus, from here, our work focuses only on the horizontal components of the surface displacement.

4. Results

4.1. Horizontal surface displacement maps

Horizontal surface displacement measured from OIC along the 2021 Maduo earthquake show dominant East-West component, with relative amplitude reaching ±2 m (Fig. 1a), while the North-South component, when excluding the high-displacement geomorphic artefacts, is limited to ±1 m and is only detectable in a few places (Fig. 1b). This is consistent with the left-lateral strike-slip motion determined from seismological and geodetic data (Fan et al., 2022; K. He et al., 2021; Q. Li et al., 2022; Wang et al., 2021; Wei et al., 2022; Zhang et al., 2022; Jin and Fialko, 2021; C. Li et al., 2022; Li et al., 2023; Liu et al., 2022; Xiong et al., 2022; Xu et al., 2021, 2021; Yang et al., 2022; Zhao et al., 2021), and from field observation (Pan et al., 2022; Ren et al., 2022, 2021; Xie et al., 2022; Yuan et al., 2022). The area affected by surface deformation during the 2021 Maduo event, referred to as the FZ, is clearly visible in the OIC results, and its geometry is consistent with the field rupture mapping (Fig. 1b). The FZW corresponds to the width of the area showing a gradient of displacement between the two sides of the fault, as seen on the across-fault displacement profiles (Fig. 2). FZW varies significantly along the rupture, including narrow FZs that correlate with the localized ground ruptures (red lines, Fig. 1b), and wide FZs, from few hundreds of meters to kilometers, that correspond to regions of distributed fracturing (orange lines, Fig. 1b) or rupture gaps (no visible ground ruptures, Fig. 1b). Rupture azimuth variations associated with local geometrical asperities are also found all along the Maduo FZ, with three main distinct sections that are separated by two major fault bends, respectively located at longitude 97.9°E and 99.0°E. The central section strikes WNW-ESE (~N105), whereas the Eastern and Western sections strike E-W (~N84 and ~N94, respectively).

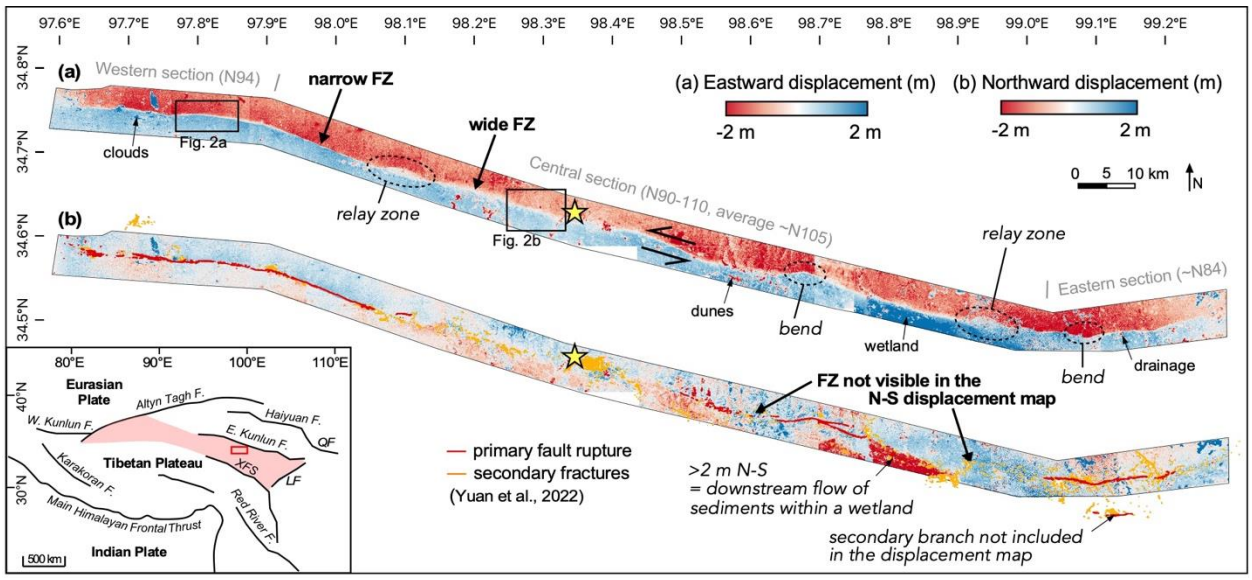

Figure 1: (a) East-West and (b) North-South surface displacement along the 2021 Maduo rupture measured at 0.5 m gsd from the correlation of pre-earthquake SPOT6/7 images and post-earthquake Pleiades images (see methodology for gsd details). The Fault Zone (FZ) appears as a continuous and curvilinear structure separating the NE and the SW blocks. Some geometrical complexities, including bends and relay zones, are indicated using dashed-line circles. Examples of artefacts related to geomorphic or meteorologic processes are indicated using thin black arrows. Epicenter location, from global CMT catalog (GCMT), is shown with a yellow star. Field rupture map from Yuan et al., 2022 is overlaid in (b) with, in red, the primary ruptures, and in orange, the secondary fractures. Inset at the bottom left shows the tectonic context, modified from Ren et al. (2022). Light red area is the Bayan Har block. Red box is the area of (a). LF is the Longmenshan Fault. XFS is the Xianshuihe Fault System. QF is the Qinling Fault.

4.2. Separating the localized, distributed and diffuse components of the deformation

We use stacked profiles to analyze how the fault-parallel surface displacement distributes between the localized deformation on faults, the distributed deformation on fractures, and the diffuse deformation. Stack boxes are 200-m wide, and displacement results are stacked within the boxes using a weighted median method that uses the output OIC correlation score. Fault-parallel displacement is derived from the combination of the East-West and North-South displacement along the stack profile with respect to the local fault azimuth (StackProf software).

4.2.1. Individual profile analysis

Individual profile analysis is performed following the method of Antoine et al. (2021, 2022) to measure the localized, distributed and diffuse components of the deformation. Similar methods are widely used to characterize earthquake surface deformation based on OIC results, though profile widths and lengths can vary (Ajorlou et al., 2021; Barnhart et al., 2020; Delorme et al., 2020; Gold et al., 2015; Li et al., 2022; Milliner et al., 2016; Scott et al., 2018). In this study, similar to Antoine et al. (2021, 2022), the length of profiles ranges from 1 (Fig. 2a) to 5 (Fig. 2b) km, allowing to capture the horizontal trend outside of the diffuse deformation zone, corresponding to the far-field elastic response of the media. Far-field elastic repones is usually fit by an arctangent function (Segall, 2010) though, because of the limited ±5 km coverage of the OIC results around the faults, it appears as an horizontal trend in the profiles.

We quantify the variations in the slope along the across-fault displacement profile, referred to as displacement gradient, which reveal variations in the underlying mechanisms of deformation across the FZ. For example, along profile AA' (Fig. 2a), highest displacement gradient of 2.4% is observed in the center of the profile from -40 m to +10 m. This region correlates with the

location of a primary fault mapped in the field (black line, Fig. 2a), and thus corresponds to the localized surface deformation. The localized deformation area is clearly separated from the surrounding regions that exhibits a displacement gradient of 0.5%, and can correlate with distributed fractures in the field. We refer these second regions as the distributed deformation regions. A third region can also be distinguished on the northern side of the profile, from -175 to -345 m, where the displacement gradient approaches 0.3%. This region clearly does not show any apparent association with field-mapped fractures thus we classify it as diffuse deformation. Diffuse deformation is also inferred along the BB' profile, where 1.48 m of left-lateral displacement is accommodated with a uniform displacement gradient of 0.1% (-250 to +700 m, Fig. 2b), and across a region where only few sparse secondary fractures were identified in the field.

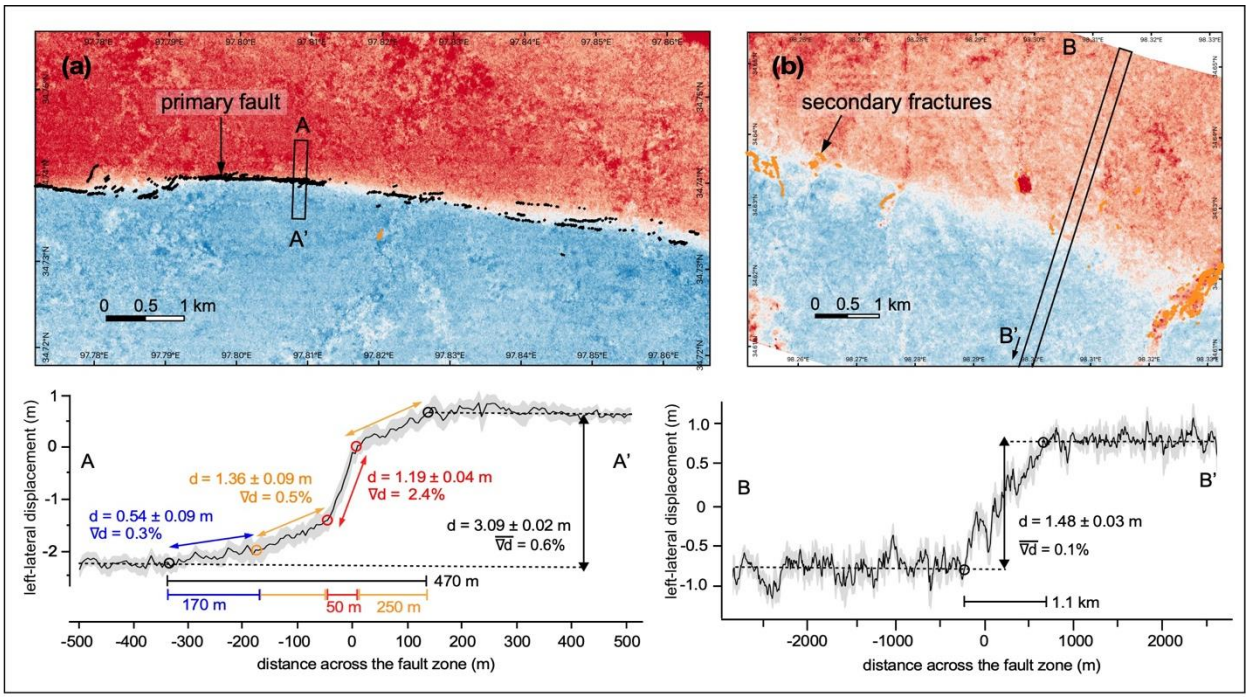

Figure 2: Zoom in the East-West displacement map in (a) a region of primarily distributed deformation, and (b) a region of primarily diffuse deformation. Rupture map is from Yuan

et al. (2022). AA' and BB' across-fault displacement profiles are presented below the displacement maps. For each profile, the values of displacement *d*, the width over which this displacement occurs (horizontal bars), and the corresponding displacement gradient ∇d is indicated for the total (black), localized (red), distributed (orange) and diffuse (blue) deformation regions.

4.2.2. Surface displacement budget associated with the total, localized, distributed, and diffuse deformations

We measure the evolution of fault-parallel displacement along the rupture strike from the analysis of 781 cross-fault profiles located every 200 m, together with the field rupture map from Yuan et al. (2022). Using the same method as in Figure 2, within each of the 781 profiles, we measure the surface displacement offset associated with the total (black curve; Fig. 3a,b), localized (red area; Fig. 3a), and distributed deformations (light orange area; Fig. 3a). The diffuse deformation (blue area; Fig. 3a) is then calculated from the difference between the total displacement curve and the sum of the localized and distributed deformations.

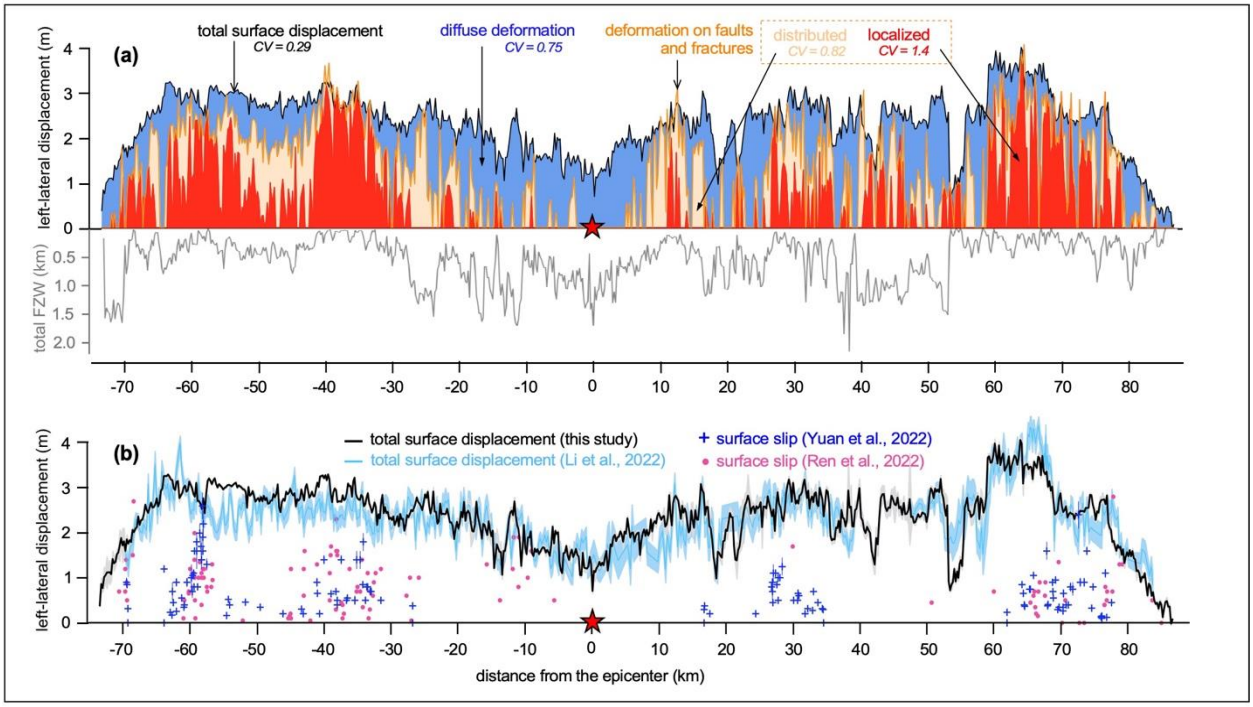

298

299 **Figure 3: (a) Complete surface displacement budget for the 2021 Maduo rupture (top plot).**
300 **Black curve is the total surface displacement. Orange curve includes the displacement**
301 **occurring on primary faults (red area) and secondary fractures (light orange area). Diffuse**
302 **deformation corresponds to the blue area. Fault Zone Width (FZW) is shown in the bottom**
303 **plot with the grey curve. The coefficient of variation (CV) reflects the degrees of variability**
304 **of the curves, and is defined as the ratio between the standard deviation and the mean. (b)**
305 **Comparison between total displacement measured from optical OIC (curves) and faults**
306 **offsets measured in the field (points and crosses), in the left-lateral component, along the**
307 **2021 Maduo rupture. Black curve is from this study, and blue curve is from Li et al. (2022)**
308 **who used Sentinel-2B images at 10 m gsd.**

309

310 Our results first show that the total surface displacement associated with the 2021 Maduo rupture
311 ranges between 1 and 4 m (to the exception of the two rupture tips where displacement tapers to

312 zero), with the smallest displacement values reported in the epicentral region (-20 to +10 km). In
313 comparison, the largest surface displacement is measured along the eastern and western sections
314 of the rupture. On average, total surface displacement is 2.35 ± 0.09 m, and occurs over a total
315 FZW of 30 to 2215 m, which corresponds to an average total FZW of 600 m. Coefficient of
316 variation (CV) of the total displacement curve is 0.29, which is unexpectedly small considering
317 the complexity of the ruptures and the scattering of the field offsets (Fig. 3b; Pan et al., 2022;
318 Ren et al., 2022, 2021; Xie et al., 2022; Yang et al., 2022; Yuan et al., 2022). Localized
319 deformation, occurs primarily along the eastern (30 to +80 km) and western sections (-30 to -70
320 km), with no or few offsets detected along the central region of the rupture. The localized
321 deformation, on the other hand, when average along the 2021 Maduo rupture length, represents
322 0.62 ± 0.05 m, so 26.3% of the total surface displacement, and occurs over an average width of
323 87 m. The localized deformation curve represents the maximum envelop of the field data, as it is
324 usually observed for optical studies (e.g., Antoine, 2021; Milliner, 2015). The CV of the
325 localized deformation curve is 1.4, which reflects the complexity and discontinuity of the surface
326 ruptures, as evidenced in the field.
327
328 Distributed deformation is detected essentially along the eastern and western sections of the
329 Maduo rupture, and primarily alongside or at the tips of the primary fault ruptures. On average,
330 the distributed deformation is 0.67 ± 0.09 m, corresponding to 28.5% of the total surface
331 displacement budget, and occurs over an average width of 133 m around the localized
332 deformation regions. The CV of the distributed deformation curve is 0.82. Very few distributed
333 deformation is detected in the epicenter area, similar to what was observed for the localized
334 deformation. In fact, the epicenter area is mainly characterized by diffuse deformation as shown

by profile BB' (Fig. 2b). In contrast with the localized and distributed deformations, the diffuse deformation is found along most of the rupture length (blue area, Fig. 3a). It has the largest amplitudes along the epicentral area, up to ~2 m, and at the rupture tips. The average surface displacement associated with the diffuse deformation component is 1.06 ± 0.09 m, representing 45.2% of the total surface displacement. The CV for the diffuse deformation curve is 0.75, which is intermediate to that of the distributed and total displacement curves. The contrasts between amplitudes and CVs of the different displacement curves thus reveal the crucial role of the distributed and diffuse deformations in accommodating the total co-seismic surface displacement in regions of lesser surface fault slip (Antoine et al., 2022).

4.2.3. Evolution of the FZW

The total FZW corresponds to the width of the total displacement offset, and is reported for each of the 781 profiles (grey curve, Fig. 3a). For example, along the profiles AA' and BB' (Fig. 2), total FZW is 480 and 1.1 km, respectively. Along the Maduo rupture, the largest FZWs, up to 2.15 km, are found in the epicenter area, and in part of the SE section (+35 to +53 km). Along the SE section, however, the rupture propagated across swampy terrains (indicated as wetland in Fig. 1) and the trace of the rupture might not have been all well preserved, leading to a possible over-estimation of the total FZW. Nevertheless, the lowest FZWs are found essentially along the NW and SE sections, from -65 to -30 km and +60 to +80 km. Interestingly, the epicentral area also corresponds to the area of smallest surface displacement along the 2021 Maduo rupture, whereas the NW and SE sections have the greatest surface displacement. Hence, we observe a decrease of the FZW together with an increase of the displacement, which is in contradiction with what has been previously reported in field studies (Faulkner et al., 2011; Savage and

Brodsky, 2011). This is likely due to that field studies most often describe only the off-fault fractures affecting the first tens to hundreds of meters around the faults, which are associated with dynamically activated off-fault damage that tend to increase in width with slip on the fault (Faulkner et al., 2011; Okubo et al., 2019; Thomas and Bhat, 2018). Here, measurements of the surface deformation are performed at a wider (>0.5 km) scale, and include the diffuse deformation as part of the FZ deformation budget. The decrease of the total FZW with increasing displacement thus highlights the decreasing contribution of the diffuse deformation with increasing coseismic surface displacement, as inferred in previous studies (Antoine et al., 2021; Perrin et al., 2016).

4.3. Displacement gradient analysis

4.3.1. Localized, distributed, and diffuse displacement gradients

We derive the displacement gradient ∇d, as a first order equivalent of strain, for each deformation region across the FZ from the separate analysis of the displacement values and widths for the localized, distributed and diffuse deformation regions. Examples are given along the profiles AA' and BB' (Fig. 2), and a similar approach is applied to each of the 781 across-fault profiles (Fig. 4a). Careful examination of each profile shows that the regions characterized entirely by diffuse deformation, including the epicentral area, are associated with across-fault displacement gradients below 0.3% (e.g., $\nabla d = 1.48/1100 = 0.0013$ in profile BB'). Statistical analysis shows a median displacement gradient value of 0.2% for the diffuse deformation regions with a lower (Q1) and upper (Q3) quartile values of 0.1 and 0.5%, respectively (blue barplot, Fig. 4a). Distributed deformation is associated with a median displacement gradients of 0.5%, and a Q1 and Q3 values of 0.3 and 1% (orange barplot, Fig. 4a). As an example, along the profile

AA' the distributed deformation shows a ∇d = 1.36/250 = 0.0054. Finally, displacement gradients associated with the localized deformation dominantly range between 1.2% (Q1) and 3% (Q3), (e.g., ∇d = 1.19/50 = 0.024 in profile AA', Fig. 2a ; and red barplot in Fig. 4a). All these values are in general consistent with the results from Li et al. (2023), who detected shear strains of 0.7-5% in the regions identified as localized and/or distributed deformation. Using Sentinel-2 OIC results from Li et al. (2022), Zhao et al. (2023) also measure shear strain over the diffuse deformation regions as low as 0.1-0.2%. In the following, the lower and upper quartiles of the distributed deformation are used thresholds expressing transitions between the different deformation regimes (Fig. 4c).

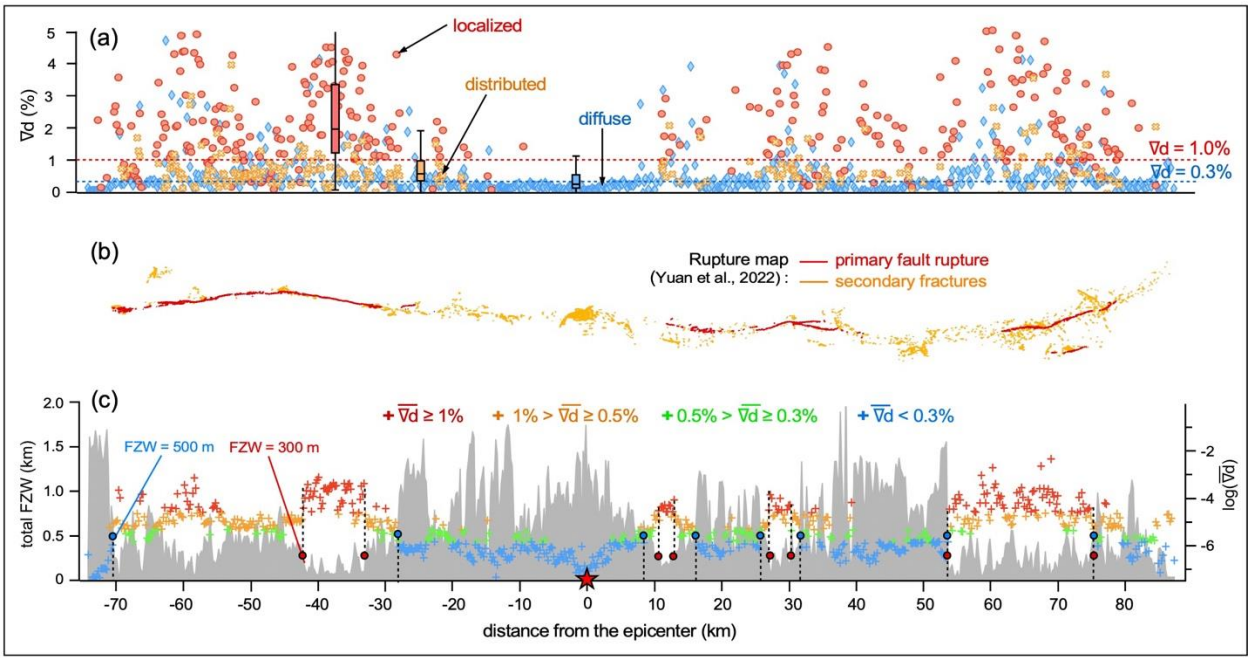

Figure 4: (a) Displacement gradients ∇d measured across the localized (red), distributed (orange) and diffuse (blue) deformation regions along the 2021 Maduo rupture. Barplots show the lower quartile (Q1), median, and upper quartile (Q3) for the ∇d measurements of the corresponding components. Blue and red dashed lines respectively highlight the

transitions between diffuse and distributed, and distributed and localized deformation regimes. (b) Field map of the 2021 Maduo surface rupture including, in red, the primary faults, and in orange, the secondary fractures (Yuan et al., 2020). (c) Evolution of the total FZW (grey area, Fig. 3a) and average displacement gradient across the FZ (colored crosses). Color scale reflects the different ranges of displacement gradients as assessed in (a). Distributed deformation is separated in two, with the value of 0.5% representing the theoretical inelastic deformation threshold (Barnhart et al., 2020). Red and blue dots highlight, in the FZW curve, some examples of transitions from a primarily diffuse to a primarily localized surface deformation, occurring for corresponding FZW values of 300 to 500 m. In (a), each profile can be represented by 1 to 3 points with each point corresponding to a different deformation mode, whereas in (c), each profile is represented by 1 point that reflects the dominant deformation mode.

4.3.2. Average displacement gradients as a measure of the dominant mode of deformation

Calculating the ratio between the total displacement offset and the total FZW for each profile, we analyze the evolution of the average displacement gradient $\overline{\nabla d}$ along the Maduo rupture, and assess along-strike evolutions in the dominant mode of deformation (Fig. 4c). As an example, in the case of profile AA' (Fig. 2a), the dominant mode of deformation is the distributed deformation (accounting for 1.36±09 m of offset along that profile), which is consistent with a $\overline{\nabla d}$ of 0.54%, that falls into the class of 0.3-1% inferred previously for the distributed deformation mode. Similarly, in the case of profile BB' (Fig. 2b), the unique mode of deformation is the diffuse deformation, and is associated with $\overline{\nabla d}$ of 0.13%, which is within the range of 0.1-0.3% identified as characteristic of the diffuse deformation. Within the range of 0.3-

1% that corresponds to the distributed deformation, we additionally distinguish the range 0.3-0.5%, and 0.5-1%, with 0.5% being the theoretical inelastic deformation usually considered (e.g., Barnhart et al., 2020; Rodriguez Padilla et al., 2022; Scott et al., 2018). Though, in our results, there is no clear difference between the patterns associated with the 0.3-0.5% and the 0.5-1% ranges, and fractures could be observed starting from 0.3%.

Results from the average gradient analysis (Fig. 4b) show that the localized deformation is dominant along most of the primary fault sections, whereas diffuse deformation is dominant along the rupture gaps. This is consistent with our previous surface displacement measurements (Fig. 3a), as well as with the field observations (Figs. 3b and 4b). Hence, $\overline{\nabla d}$ can be used as a parameter to characterize the dominant mode of surface deformation along the 2021 Maduo rupture, along with the more local metric of ∇d that characterizes each deformation mode separately. Each of these different metrics are used hereafter to analyze the behavior of the different deformation components, and to assess possible underlying mechanisms.

4.4. Evolution of the width of the localized, distributed, and diffuse deformation zones and total FZW

We analyzed the evolution of the width of the localized, distributed, and diffuse deformation zones with respect to their contributions to the surface displacement budget (Figs. 5a and S6). Results show that the width of the diffuse deformation zone increases with increasing amplitude of the diffuse deformation (blue crosses and curve). This increasing trend is best fit (by minimizing the r^2 norm) using an exponential relation, which is coherent with observations from experiments of microcrack development and fracture growth (Chen et al., 2021; Long et al., 2021; J. A. McBeck et al., 2021). The maximum width of the diffuse deformation zone detected

for the 2021 Maduo earthquake is ~2 km, which also corresponds to the maximum value obtained for the total FZW. In comparison, the width of the localized deformation zone also increases with increasing amplitude of the localized deformation (red crosses and curve) but follows a logarithmic trend, coherent with existing field observations (e.g., Chester et al., 2005; Mitchell and Faulkner, 2009; Savage and Brodsky, 2011). The width of the localized deformation region reaches a maximum of about 100 m for any value of localized displacement about 1.5m or larger. Here, contrasts between the governing equation of FZW with displacement for the localized and diffuse deformation demonstrates that these two modes of deformation are controlled by different underlying mechanisms. Finally, the width of the distributed deformation domain increases linearly with increase distributed deformation, with a maximum detected width of ~500 m (orange crosses and curve). Distributed deformation then appears as a transition mechanism between the diffuse and localized deformations, consistent with the fact that the distributed deformation occurs spatially at the transition between the localized and distributed deformation regions (Figs. 2a and 3a) and is associated with intermediate values of ∇d (Fig. 4).

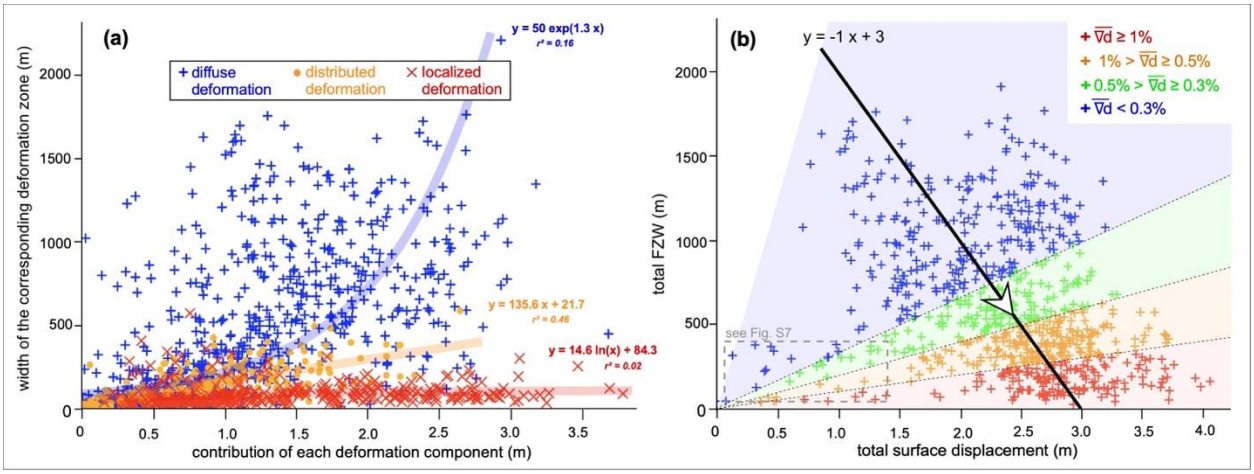

Figure 5: Scatterplots of evolution of deformation zone width with displacement based on the analysis of the 781 across-fault displacement profiles (Figs. 2c and 3). (a) Evolution, for

each deformation process, of the deformation region for the corresponding displacement amplitude. Similar to Figure 4a, each profile is represented by 1 to 3 points. Thick lines propose possible evolution laws for each type of surface deformation. (b) Evolution of the total FZW with increasing total surface displacement. Color code highlights the dominant surface deformation mode, similarly to Figure 4c. Black line and white arrow highlight the decrease in total FZW with increasing total surface displacement.

Considering all the contributions to the surface displacement together, we observe an overall decrease of the total FZW with increasing total surface displacement (black line with white arrow, Figure 5b), as previously inferred from the analysis of FZW and displacement measurements along the rupture strike (Fig. 3a). Overlapping this result with the average displacement gradient $\overline{\nabla d}$ ranges (color scale, Fig. 5b), we observe a decrease in the total FZW that correlates with the increase in $\overline{\nabla d}$, and thus with a greater contribution of the localized deformation on faults with regard to that of the distributed and diffuse deformations. Hence, we propose that two mechanisms are at play here. First, the evolution of the total FZW is controlled by the ratio of the diffuse, on one hand, and localized and distributed, on the other hand, deformation contributions to the total displacement budget (Fig. 5b). Second, this ratio decreases with increasing total surface displacement, as a result of greater displacement being accommodated by primary faults (Fig. 3a).

Still, several points corresponding to both the lowest displacement and FZW values (grey dashed box, Fig. 5b) remain outside of this decreasing trend, and tend to show a positive relation between total surface displacement and FZW. We suggest this pattern to be characteristic of

483 regions with the smallest displacement values, located at the rupture tips, and experiencing the
484 development of the diffuse deformation zones. This is indeed suggested by geological field
485 observations (Faulkner et al., 2011; Manighetti et al., 2004; Perrin et al., 2016) that describe
486 wider off-fault damage in regions of fault growth. We confirm this inference by separating the
487 points from Figure 5b based on their locations along the rupture strike (Fig. S7). Points that
488 describe this increasing relation are mostly located along the SE rupture tip (blue cercle, Fig. S7),
489 which is characterized primarily by surface diffuse deformation (Fig. 3a). The NW tip (green
490 circle, Fig. S7), though, shows a decrease in total FZW with increasing displacement, consistent
491 with the other regions of the rupture. This contrast between the NW and SE rupture tips may
492 reflect different mechanical behaviors between the NW and SE rupture tips due to the contrasts
493 in fault maturity as suggested by Li et al. (2023). Geological field observations indeed show
494 lower accumulated fault displacement along the SE side of the Jiangcuo fault, as a consequence
495 of the eastward long-term fault propagation (Li et al., 2022; Pan et al., 2022), thus in favor of
496 greater diffuse deformation.
497
498 ## 5. Discussion
499 ### 5.1. Diffuse inelastic deformation below the rock failure stress: laboratory observations
500 Diffuse deformation along the 2021 Maduo rupture represents 45.2% of the total surface
501 displacement budget (Fig. 3a), with displacement gradients that range between 0.1 and 0.3%.
502 Such displacement gradient values are below the value of ~0.5% that is usually considered as the
503 minimum strain threshold for the occurrence of surface inelastic deformation (e.g., Barnhart et
504 al., 2020; Cheng and Barnhart, 2021; Li et al., 2023; Milliner, 2021; Scott et al., 2018). However,
505 this value is empirical and primarily based on surface observation of fractures. Laboratory

experiments of rock sample deformation in tri-axial compression, though, showed that inelastic deformation actually occurs for lower values of strain, down to ~0.1-0.2%, which is below the actual rock failure stress (e.g., Dong et al., 2023; Lockner, 1998; McBeck et al., 2022, 2021; Thompson et al., 2006; Fig. 6a,b). Such deformation occurs through diffuse microfracturing (phase i, Fig. 6a) for stresses below 75-90% of the failure stress, and before the deformation starts to localize along a defined fault plane (phase j and k, Fig. 6a). This microfracturing is characterized by independent microcracks, homogeneously distributed through the rock sample. Considering that we measure the displacement across the sample, it would bear a similar pattern as the one we observed in the diffuse regions of the Maduo rupture, that is a continuous surface displacement gradient across the FZ. These strong similarities between the deformation patterns described in laboratory experiments and the diffuse deformation patterns observed along the 2021 Maduo rupture then strengthen our initial hypothesis which is: surface diffuse deformation along the 2021 Maduo rupture is an inelastic process, and corresponds to diffuse plastic yielding of the off-fault medium below the shallow FZ failure stress.

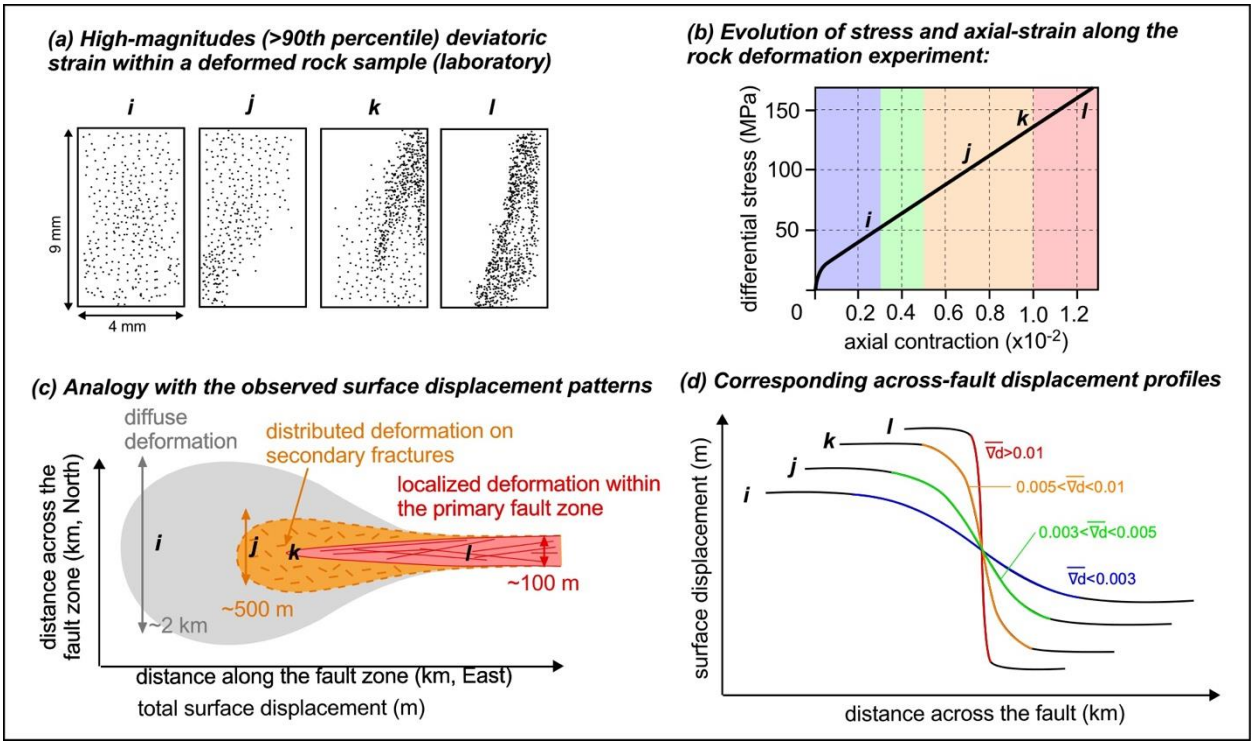

521

522 **Figure 6: Comparison between (a,b) observations of rock deformation from tri-axial**
523 **compression of rock sample in laboratory (mod. from McBeck et al., 2022) and (c,d)**
524 **observations of surface deformation along the 2021 Maduo rupture. (a) View in cross-**
525 **section of the highest-magnitude deviatoric strain values (black points) distribution across**
526 **the rock sample during the experiment, and (b) corresponding stress versus axial-strain**
527 **relation. Color code in (b) highlights the different classes of strain inferred from the $\overline{\nabla d}$**
528 **analysis (see Fig. 4). Letters (i-l) highlight corresponding stages of deformation in (a) and**
529 **(b). (c) Idealized sketch, based on our surface observations along the 2021 Maduo rupture**
530 **(Fig. 3a), of the evolution of the FZ deformation with increasing total surface displacement,**
531 **from (i) a diffuse to (l) a localized deformation mode, through (j,k) a region of mixed**
532 **deformation mode. (d) Surface displacement profiles across the different surface**
533 **deformation regions (i-l) in (c). In (b,d), color code highlights the different classes of $\overline{\nabla d}$**
534 **(see Fig. 4).**

Bimodal evolution of $\overline{\nabla d}$ with total displacement (Fig. 7a) and total FZW is also observed (Fig. 7b), supporting the co-existence of two different mechanical processes along the 2021 Maduo rupture. On one hand, the diffuse deformation gradient (blue points, Fig. 7) has little sensitivity to variations in the coseismic displacement, highlighting the stable behavior of plastic yielding, but also its low-energy efficiency. Conversely, within the dominantly localized deformation regions (red points, Fig. 7), the displacement gradient has great sensitivity to increases in the displacement gradients, which is consistent with the unstable nature of dynamic fault slip (Collettini et al., 2011; Ikari et al., 2011). Such increase in $\overline{\nabla d}$ in the localized deformation regions do not lead to significant changes in the FZW, showing the ability of the localized deformation to concentrate large amounts of deformation within confined regions, hence representing a highly energy-efficient deformation regime.

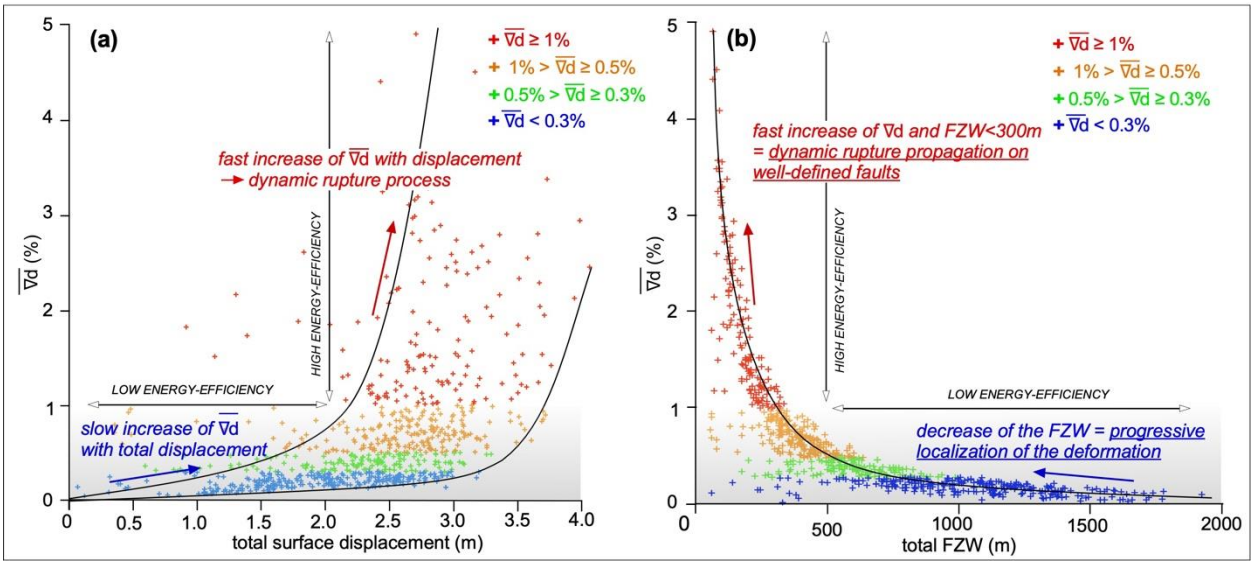

Figure 7: Evolution of the average displacement gradient $\overline{\nabla d}$ with (a) the total surface displacement, and (b) the total FZW. Color code highlights the different classes of $\overline{\nabla d}$

including the localized (red), distributed (orange and green), and diffuse (blue) deformations (Fig. 4c). Trends in the data are highlighted with black lines and colored arrows.

Such comparison between a natural rupture and crystalline rock samples being deformed in the laboratory, is also supported by other deformation experiments in granular porous medium (Aben et al., 2017; Baud et al., 2000; Cilona et al., 2012; Fossen et al., 2007; Visage et al., 2023), as well as field observations (Aubert et al., 2020; Cilona et al., 2012; Micarelli et al., 2006), strengthening our previous interpretations. In the case of the 2021 Maduo rupture, indeed, lithology consists in granular porous carbonate rocks overlaid with unconsolidated quaternary sediments at some locations (Ren et al., 2021; Yuan et al., 2022), which differ from the crystalline nature of the rock used in the experiments described previously. Added to the low-pressure conditions of the shallow crust and interactions with the free-surface, plastic deformation processes can differ from that described previously. In this case, shear and/or dilatation deformation bands (Aben et al., 2017; Aubert et al., 2020; Fossen et al., 2007; Micarelli et al., 2006; Visage et al., 2023), and possibly viscous cataclastic flow (Baud et al., 2000; Cilona et al., 2012) have been suggested as the primarily plastic deformation mechanisms, in addition to the microfracturing occurring in the most consolidated, e.g., cemented and/or healed, regions (Micarelli et al., 2006).

5.2. Relations with shallow FZ frictional strength, and the dynamic rupture process

Diffuse deformation along the 2021 Maduo rupture contributes to almost the entire surface displacement budget along the epicentral area, whereas is it a minor component of the surface

574 displacement along the NE and SW rupture sections (Fig. 3a). Based on the previous inference
575 that the diffuse deformation corresponds to plastic yielding below the FZ failure stress (section
576 5.1), it implies that the dynamic stresses due to coseismic rupture in the epicentral area did not
577 overcome the shallow FZ frictional strength. Instead, the stresses associated with the earthquake
578 rupture induced a widespread plastic yielding, which manifests as broad surface diffusive
579 deformation with little surface ruptures.
580
581 Indeed, kinematic slip inversion of the 2021 Maduo event revealed a bilateral pulse-like rupture,
582 with the epicenter area that only slipped during the first 5-8 seconds of the ~40 seconds-long
583 earthquake rupture (Chen et al., 2022; Yuan and Li, 2023; Zheng et al., 2023). Such rupture
584 process resulted in lesser co-seismic displacement in the epicenter area both at depth and at the
585 surface (Hirakawa and Ma, 2016; Wang and Day, 2017), thus showing good correspondence
586 with the patterns we observed at the surface (Fig. 3). The nucleation patch was inferred to be 5~8
587 km wide, and confined within the first 10 km of the crust, supporting the hypothesis of a blind
588 fault rupture and associated surface diffuse deformation. After the first 5-8 seconds, the pulse-
589 like rupture takes over and propagates bilaterally along the fault plane. The propagation is
590 associated with an increase in the slip patch width and amplitude with increasing distance to the
591 epicenter, until it reaches the maximum fault width and ruptures the ground surface. Based on
592 the seismic and geodetic data (e.g., Jin and Fialko, 2021; Liu et al., 2022; Wei et al., 2022; Yuan
593 and Li, 2023; Yue et al., 2022; Zheng et al., 2023; Figs. 1 and 3), and the field observations (Pan
594 et al., 2022; Ren et al., 2022, 2021; Xie et al., 2022; Yuan et al., 2022), the rupture reached the
595 surface at ~30 km on either side of the epicenter. Such rupture process, coupled with shallow FZ

596 frictional strength contrast, would result in smaller shallow coseismic slip and more diffusive
597 deformation in the epicentral area, compared to the NW and SE rupture sections.
598
599 The hypothesis of a stronger shallow FZ frictional strength in the epicenter area is partially
600 supported by the Jiangcuo fault being an immature fault with low slip rate (Pan et al., 2022; Ren
601 et al., 2021) and low accumulated deformation (Li et al., 2022). Locally such frictional strength
602 could also be enhanced by the significant presence of sediments, including quaternary sand-
603 dunes or swampy terrain were observed (Yuan et al., 2022), which typically lead to velocity-
604 strengthening behavior (Ikari et al., 2011; Scholz, 1998). Part of the diffuse deformation also
605 occurred within an area of bedrock (+10 to +25 km SE from the epicenter), but the latter is
606 associated with the highest presence of drainages across the FZ (Yuan et al., 2022), which
607 suggests the presence of recent unconsolidated and wet sediments at the surface. As shown by
608 Hirakawa and Ma (2016), the presence of sediments and/or water could also facilitate the
609 development of a pulse-like rupture, consistent with kinematically constrained rupture process.
610
611 One question about the surface diffuse deformation measured along the epicentral area is
612 whether it relates to the postseismic response of a shallow compliant FZ to a blind fault rupture
613 at depth (Fialko et al., 2002). In this case, one would expect shallow creep to account for this
614 surface elastic deformation. However, shallow afterslip along the 2021 Maduo rupture reaches
615 only ~0.2 m after 1 year (He et al., 2021; Jin and Fialko, 2021; Xiong et al., 2022; Zhao et al.,
616 2021; Zhao et al., 2023). Considering the exponential decrease of afterslip with time, it is thus
617 very unlikely that the shallow layers will account for the 1.5 m of diffuse deformation (Jin et al.,
618 2023). In addition, a majority of this shallow afterslip occur at depth of 2-3 km (Jin et al., 2023),

which suggests the surface afterslip is less likely and supports the hypothesis of bulk plastic yielding within the top 1-2 km of the crust. Added to the fact that few sparse fractures were detected at the surface in this region (Figs. 1, and 2b; Liu et al., 2023), showing that inelastic deformation did reach the surface in this area, the diffuse bulk plastic behavior then seems like a reasonable interpretation of the surface diffuse deformation.

Conclusions

In this work, we present high-resolution measurements of the surface displacement field along the 2021 M_w7.4 Maduo, Tibet, rupture, obtained from the sub-pixel cross-correlation of Pleiades and SPOT6/7 satellite images. These measurements allow for a detailed quantification of the surface displacement along the Maduo fault zone, including the separation of the localized deformation along primary faults, the distributed deformation on secondary fractures, and the bulk diffuse deformation. Results show that diffuse deformation contributed to up to ~45% of the total surface deformation, and generated continuous ground deformation across regions as wide as 2 km. Diffuse deformation is the dominant process within the first 30 km around the earthquake epicenter, whereas other regions of the rupture are primarily characterized by distributed and localized deformations. Our analysis reveals different governing equations for the localized, distributed, and diffuse deformations, suggesting different underlying mechanisms. Comparison with existing laboratory observations of rock deformation, also supported by field and seismic observations, suggest that diffuse deformation corresponds to bulk plastic yielding occurring in regions where the dynamic stresses did not overcome the shallow fault zone frictional strength. Conversely, the localized deformation occurs in regions where the dynamic rupture propagation could be sustained. In the case of the 2021 Maduo rupture, lower dynamic

stresses associated with the nascent-pulse-like rupture, combined with greater shallow fault zone strength possibly due to the presence of unconsolidated and/or wet sediments, would favor such shallow diffuse bulk plastic yielding along the epicenter area.

Acknowledgments

This work was carried out at the Jet Propulsion Laboratory, California Institute of Technology, under a contract with the National Aeronautics and Space Administration. This work was supported by NASA Decadal Survey Incubator/Surface Topography and Vegetation program, and partly supported by TOSCA CNES and the ANR-18-CE31-0012 projects. This study contributed to the IdEx Université de Paris ANR-18-IDEX-0001. Numerical computations were performed on the GATTACA (JPL, USA), and S-CAPAD/DANTE (IPGP, France) platforms.

Open Research

The Pleiades images were provided by the CEOS Seismic Hazards Pilot from ESA (http://ceos.org/ourwork/workinggroups/disasters/earthquakes; last accessed on 01/03/24) and the DINAMIS program from CNES (https://dinamis.teledetection.fr; https://cnes.fr; last accessed on 01/03/24). The SPOT6/7 images were provided by the DINAMIS program and ForM@Ter pole (https://en.poleterresolide.fr; last accessed on 01/03/2024) from CNES. Sentinel2 images were accesses at https://dataspace.copernicus.eu/ (last accessed on 01/03/24). MicMac (https://github.com/micmacIGN/micmac; last accessed on 01/03/24) and StackProf (https://github.com/IPGP/stackprof; last accessed on 01/03/24) are open source. Supplementary figures providing details on the methodology and on the results of this study are available in the

electronic. Surface displacement maps, and fault displacement measurements will be available for the published version of the manuscript.

References

Aben, F.M., Doan, M.-L., Gratier, J.-P., Renard, F., 2017. High strain rate deformation of porous sandstone and the asymmetry of earthquake damage in shallow fault zones. Earth Planet. Sci. Lett. 463, 81–91. https://doi.org/10.1016/j.epsl.2017.01.016

Ajorlou, N., Hollingsworth, J., Mousavi, Z., Ghods, A., Masoumi, Z., 2021. Characterizing near-field surface deformation in the 1990 Rudbar earthquake (Iran) using optical image correlation. Geochem. Geophys. Geosystems 22, 2021 009704. https://doi.org/10.1029/2021GC009704

Alongi, T., Brodsky, E.E., Kluesner, J., Brothers, D., 2022. Using active source seismology to image the Palos Verdes Fault damage zone as a function of distance, depth, and geology. Earth Planet. Sci. Lett. 600, 117871. https://doi.org/10.1016/j.epsl.2022.117871

Antoine, Klinger, Y., Delorme, A., Wang, K., Bürgmann, R., Gold, R.D., 2021. Diffuse Deformation and Surface Faulting Distribution from Submetric Image Correlation along the 2019 Ridgecrest, California, Ruptures. Bull. Seismol. Soc. Am. 111, 2275–2302. https://doi.org/10.1785/0120210036

Antoine, S.L., Klinger, Y., Delorme, A., Gold, R.D., 2022. Off-Fault Deformation in Regions of Complex Fault Geometries: The 2013, Mw7.7, Baluchistan Rupture (Pakistan). J. Geophys. Res. Solid Earth 127, e2022JB024480. https://doi.org/10.1029/2022JB024480

685 Aubert, I., Léonide, P., Lamarche, J., Salardon, R., 2020. Diagenetic evolution of fault zones in
686 Urgonian microporous carbonates, impact on reservoir properties (Provence – southeast
687 France). Solid Earth 11, 1163–1186. https://doi.org/10.5194/se-11-1163-2020
688 Barbot, S., Fialko, Y., Sandwell, D., 2008. Effect of a compliant fault zone on the inferred
689 earthquake slip distribution. J. Geophys. Res. Solid Earth 113.
690 https://doi.org/10.1029/2007JB005256
691 Barnhart, W.D., Gold, R.D., Hollingsworth, J., 2020. Localized fault-zone dilatancy and surface
692 inelasticity of the 2019 Ridgecrest earthquakes. Nat Geosci 13, 699–704.
693 https://doi.org/10.1038/s41561-020-0628-8
694 Baud, P., Zhu, W., Wong, T., 2000. Failure mode and weakening effect of water on sandstone. J.
695 Geophys. Res. Solid Earth 105, 16371–16389. https://doi.org/10.1029/2000JB900087
696 Budiansky, B., O'connell, R.J., 1976. Elastic moduli of a cracked solid. Int. J. Solids Struct. 12,
697 81–97. https://doi.org/10.1016/0020-7683(76)90044-5
698 Chen, K., Avouac, J.-P., Geng, J., Liang, C., Zhang, Z., Li, Z., Zhang, S., 2022. The 2021 Mw
699 7.4 Madoi Earthquake: An Archetype Bilateral Slip-Pulse Rupture Arrested at a Splay
700 Fault. Geophys. Res. Lett. 49, e2021GL095243. https://doi.org/10.1029/2021GL095243
701 Chen, L., Zhang, G., Zou, Z., Guo, Y., Zheng, X., 2021. The effect of fracture growth rate on
702 fracture process zone development in quasi-brittle rock. Eng. Fract. Mech. 258, 108086.
703 https://doi.org/10.1016/j.engfracmech.2021.108086
704 Cheng, G., Barnhart, W.D., 2021. Permanent Co-Seismic Deformation of the 2013 Mw7.7
705 Baluchistan, Pakistan Earthquake From High-Resolution Surface Strain Analysis. J.
706 Geophys. Res. Solid Earth 126, 2020 020622. https://doi.org/10.1029/2020JB020622

Chester, J.S., Chester, F.M., Kronenberg, A.K., 2005. Fracture surface energy of the Punchbowl fault, San Andreas system. Nature 437, 133–136. https://doi.org/10.1038/nature03942

Choi, J., Klinger, Y., Ferry, M., Ritz, J., Kurtz, R., Rizza, M., Bollinger, L., Davaasambuu, B., Tsend-ayush, N., Demberel, S., 2018. Geologic inheritance and earthquake rupture processes: The 1905 M ≥ 8 Tsetserleg-Bulnay strike-slip earthquake sequence, Mongolia. J Geophys Res Solid Earth 123, 1925–1953. https://doi.org/10.1002/2017JB013962

Cilona, A., Baud, P., Tondi, E., Agosta, F., Vinciguerra, S., Rustichelli, A., Spiers, C.J., 2012. Deformation bands in porous carbonate grainstones: Field and laboratory observations. J. Struct. Geol., Fault zone structure, mechanics and evolution in nature and experiment 45, 137–157. https://doi.org/10.1016/j.jsg.2012.04.012

Collettini, C., Niemeijer, A., Viti, C., Smith, S.A.F., Marone, C., 2011. Fault structure, frictional properties and mixed-mode fault slip behavior. Earth Planet. Sci. Lett. 311, 316–327. https://doi.org/10.1016/j.epsl.2011.09.020

Delorme, A., Grandin, R., Klinger, Y., Pierrot-Deseilligny, M., Feuillet, N., Jacques, E., Rupnik, E., Morishita, Y., 2020. Complex Deformation at Shallow Depth During the 30 October 2016 Mw6.5 Norcia Earthquake: Interference Between Tectonic and Gravity Processes? Tectonics 39, 2019 005596. https://doi.org/10.1029/2019TC005596

Dong, P., Xia, K., Xu, Y., Elsworth, D., Ampuero, J.-P., 2023. Laboratory earthquakes decipher control and stability of rupture speeds. Nat. Commun. 14, 2427. https://doi.org/10.1038/s41467-023-38137-w

Fan, X., Zhang, G., Zhao, D., Xie, C., Huang, C., Shan, X., 2022. Fault geometry and kinematics of the 2021 Mw 7.3 Maduo earthquake from aftershocks and InSAR observations. Front. Earth Sci. 10, 993984. https://doi.org/10.3389/feart.2022.993984

730 Faulkner, D.R., Mitchell, T.M., Healy, D., Heap, M.J., 2006. Slip on “weak” faults by the
731 rotation of regional stress in the fracture damage zone. Nature 444, 922–925.
732 https://doi.org/10.1038/nature05353
733 Faulkner, D.R., Mitchell, T.M., Jensen, E., Cembrano, J., 2011. Scaling of fault damage zones
734 with displacement and the implications for fault growth processes. J. Geophys. Res. Solid
735 Earth 116. https://doi.org/10.1029/2010JB007788
736 Fialko, Y., Sandwell, D., Agnew, D., Simons, M., Shearer, P., Minster, B., 2002. Deformation on
737 Nearby Faults Induced by the 1999 Hector Mine Earthquake.
738 https://doi.org/10.1126/science.1074671
739 Fialko, Y., Sandwell, D., Simons, M., Rosen, P., 2005. Three-dimensional deformation caused
740 by the Bam, Iran, earthquake and the origin of shallow slip deficit. Nature 435, 295–299.
741 https://doi.org/10.1038/nature03425
742 Fossen, H., Schultz, R.A., Shipton, Z.K., Mair, K., 2007. Deformation bands in sandstone: a
743 review. J Geol Soc 164, 755–769. https://doi.org/10.1144/0016-76492006-036
744 Gold, R.D., Reitman, N.G., Briggs, R.W., Barnhart, W.D., Hayes, G.P., Wilson, E., 2015. Onand
745 off-fault deformation associated with the September 2013 Mw 7.7 Balochistan
746 earthquake: Implications for geologic slip rate measurements. Tectonophysics 660, 65–
747 78. https://doi.org/10.1016/j.tecto.2015.08.019
748 Gombert, B., Duputel, Z., Jolivet, R., Doubre, C., Rivera, L., Simons, M., 2018. Revisiting the
749 1992 Landers earthquake: a Bayesian exploration of co-seismic slip and off-fault damage.
750 Geophys. J. Int. 212, 839–852. https://doi.org/10.1093/gji/ggx455
751 Ha, G., Liu, J., Ren, Z., Zhu, X., Bao, G., Wu, D., Zhang, Z., 2022. The Interpretation of
752 Seismogenic Fault of the Maduo Mw 7.3 Earthquake, Qinghai Based on Remote Sensing

753 Images—A Branch of the East Kunlun Fault System. J. Earth Sci. 33, 857–868.
754 https://doi.org/10.1007/s12583-021-1556-2
755 He, K., Wen, Y., Xu, C., Zhao, Y., 2021. Fault Geometry and Slip Distribution of the 2021
756 Mw 7.4 Maduo, China, Earthquake Inferred from InSAR Measurements and Relocated
757 Aftershocks. Seismol. Res. Lett. 93, 8–20. https://doi.org/10.1785/0220210204
758 He, L., Feng, G., Wu, X., Lu, H., Xu, W., Wang, Y., Liu, J., Hu, J., Li, Z., 2021. Coseismic and
759 Early Postseismic Slip Models of the 2021 Mw 7.4 Maduo Earthquake (Western China)
760 Estimated by Space-Based Geodetic Data. Geophys. Res. Lett. 48, e2021GL095860.
761 https://doi.org/10.1029/2021GL095860
762 Heap, M.J., Faulkner, D.R., Meredith, P.G., Vinciguerra, S., 2010. Elastic moduli evolution and
763 accompanying stress changes with increasing crack damage: implications for stress
764 changes around fault zones and volcanoes during deformation. Geophys. J. Int. 183, 225–
765 236. https://doi.org/10.1111/j.1365-246X.2010.04726.x
766 Hearn, E.H., Fialko, Y., 2009. Can compliant fault zones be used to measure absolute stresses in
767 the upper crust? J. Geophys. Res. 114, B04403. https://doi.org/10.1029/2008JB005901
768 Hirakawa, E., Ma, S., 2016. Dynamic fault weakening and strengthening by gouge compaction
769 and dilatancy in a fluid-saturated fault zone. J. Geophys. Res. Solid Earth 121, 5988–
770 6008. https://doi.org/10.1002/2015JB012509
771 Ikari, M.J., Marone, C., Saffer, D.M., 2011. On the relation between fault strength and frictional
772 stability. Geology 39, 83–86. https://doi.org/10.1130/G31416.1
773 Jin, Z., Fialko, Y., 2021. Coseismic and Early Postseismic Deformation Due to the 2021 M7.4
774 Maduo (China) Earthquake. Geophys. Res. Lett. 48.
775 https://doi.org/10.1029/2021GL095213

776 Jin, Z., Fialko, Y., Yang, H., Li, Y., 2023. Transient Deformation Excited by the 2021 M7.4
777 Maduo (China) Earthquake: Evidence of a Deep Shear Zone. J. Geophys. Res. Solid
778 Earth 128, e2023JB026643. https://doi.org/10.1029/2023JB026643
779 Klinger, Y., Xu, X., Tapponnier, P., Woerd, J., Lasserre, C., King, G., 2005. High-resolution
780 satellite imagery mapping of the surface rupture and slip distribution of the Mw 7.8,
781 Kokoxili earthquake, Kunlun fault, northern Tibet, China.
782 Laws, S., Eberhardt, E., Loew, S., Descoeudres, F., 2003. Geomechanical Properties of Shear
783 Zones in the Eastern Aar Massif, Switzerland and their Implication on Tunnelling. Rock
784 Mech. Rock Eng. 36. https://doi.org/10.1007/s00603-003-0050-8
785 Leprince, S., Barbot, S., Ayoub, F., Avouac, J.-P., 2007. Automatic and precise
786 orthorectification, coregistration, and subpixel correlation of satellite images, application
787 to ground deformation measurements. Geosci Remote Sens IEEE Trans On 45, 1529–
788 1558. https://doi.org/10.1109/TGRS.2006.888937
789 Li, C., Li, T., Hollingsworth, J., Zhang, Y., Qian, L., Shan, X., 2023. Strain Threshold for the
790 Formation of Coseismic Surface Rupture. Geophys. Res. Lett. 50, e2023GL103666.
791 https://doi.org/10.1029/2023GL103666
792 Li, C., Li, T., Shan, X., Zhang, G., 2022. Extremely Large Off-Fault Deformation during the
793 2021 Mw 7.4 Maduo, Tibetan Plateau, Earthquake. Seismol. Res. Lett.
794 https://doi.org/10.1785/0220220139
795 Li, Q., Wan, Y., Li, C., Tang, H., Tan, K., Wang, D., 2022. Source Process Featuring
796 Asymmetric Rupture Velocities of the 2021 Mw 7.4 Maduo, China, Earthquake from
797 Teleseismic and Geodetic Data. Seismol. Res. Lett. 93, 1429–1439.
798 https://doi.org/10.1785/0220210300

Liu, J., Hu, J., Li, Z., Ma, Z., Wu, L., Jiang, W., Feng, G., Zhu, J., 2022. Complete three-dimensional coseismic displacements due to the 2021 Maduo earthquake in Qinghai Province, China from Sentinel-1 and ALOS-2 SAR images. Sci. China Earth Sci. 65, 687–697. https://doi.org/10.1007/s11430-021-9868-9

Liu, J., Zhijun, L., Liu, X., Milliner, C., Avouac, J.-P., Padilla, A.M.R., Xu, S., Yao, W., Klinger, Y., Han, L., Shao, Y., 2023. Multifault rupture of the 2021 Mw7.4 Maduo (China) earthquake reveals fault growth toward a stress-favored orientation. Presented at the AGU23, AGU.

Liu, X., Chen, Q., Yang, Y., Xu, Q., Zhao, J., Xu, L., Liu, R., 2022. The 2021 Mw7.4 Maduo earthquake: Coseismic slip model, triggering effect of historical earthquakes and implications for adjacent fault rupture potential. J. Geodyn. 151, 101920. https://doi.org/10.1016/j.jog.2022.101920

Lockner, D., 1998. A generalized law for brittle deformation of Westerly granite. J. Geophys. Res. 103, 5107–5123. https://doi.org/10.1029/97JB03211

Long, K., Zhang, Z., Ring, U., Faulkner, D., Gamage, R.P., 2021. Microcracks development and porosity evolution in sandstone, Sichuan basin, China: an experimental approach. Bull. Eng. Geol. Environ. 80, 7717–7729. https://doi.org/10.1007/s10064-021-02420-1

Lyakhovsky, V., Ben-Zion, Y., 2008. Scaling relations of earthquakes and aseismic deformation in a damage rheology model. Geophys. J. Int. 172, 651–662. https://doi.org/10.1111/j.1365-246X.2007.03652.x

Manighetti, I., King, G., Sammis, C.G., 2004. The role of off-fault damage in the evolution of normal faults. Earth Planet Sci Lett 217, 399–408. https://doi.org/10.1016/S0012-821X(03)00601-0

822 Materna, K., Bürgmann, R., 2016. Contrasts in compliant fault zone properties inferred from
823 geodetic measurements in the San Francisco Bay area. J. Geophys. Res. Solid Earth 121,
824 6916–6931. https://doi.org/10.1002/2016JB013243
825 McBeck, J., Ben-Zion, Y., Renard, F., 2022. Volumetric and shear strain localization throughout
826 triaxial compression experiments on rocks. Tectonophysics 822, 229181.
827 McBeck, J., Ben-Zion, Y., Renard, F., 2021. Fracture Network Localization Preceding
828 Catastrophic Failure in Triaxial Compression Experiments on Rocks. Front. Earth Sci. 9.
829 McBeck, J.A., Zhu, W., Renard, F., 2021. The competition between fracture nucleation,
830 propagation, and coalescence in dry and water-saturated crystalline rock. Solid Earth 12,
831 375–387. https://doi.org/10.5194/se-12-375-2021
832 Micarelli, L., Benedicto, A., Wibberley, C.A.J., 2006. Structural evolution and permeability of
833 normal fault zones in highly porous carbonate rocks. J. Struct. Geol. 28, 1214–1227.
834 https://doi.org/10.1016/j.jsg.2006.03.036
835 Milliner, C., 2021. Bookshelf Kinematics and the Effect of Dilatation on Fault Zone Inelastic
836 Deformation: Examples From Optical Image Correlation Measurements of the 2019
837 Ridgecrest Earthquake Sequence. J. Geophys. Res. Solid Earth 126, 2020 020551.
838 Milliner, C.W.D., 2015. Quantifying near-field and off-fault deformation patterns of the 1992
839 Mw 7.3 Landers earthquake. Geochem. Geophys. Geosystems 16, 1577–1598.
840 Milliner, C.W.D., Dolan, J.F., Hollingsworth, J., Leprince, S., Ayoub, F., 2016. Comparison of
841 coseismic near-field and off-fault surface deformation patterns of the 1992 Mw 7.3
842 Landers and 1999 Mw 7.1 Hector Mine earthquakes: Implications for controls on the
843 distribution of surface strain. Geophys Res Lett 43, 10,115-10,124.
844 https://doi.org/10.1002/2016GL069841

Mitchell, T.M., Faulkner, D.R., 2009. The nature and origin of off-fault damage surrounding strike-slip fault zones with a wide range of displacements: A field study from the Atacama fault system, northern Chile. J. Struct. Geol. 31, 802–816. https://doi.org/10.1016/j.jsg.2009.05.002

Nurminen, F., Baize, S., Boncio, P., Blumetti, A.M., Cinti, F.R., Civico, R., Guerrieri, L., 2022. SURE 2.0 – New release of the worldwide database of surface ruptures for fault displacement hazard analyses. Sci. Data 9, 729. https://doi.org/10.1038/s41597-022-01835-z

Okubo, K., 2019. Dynamics, Radiation, and Overall Energy Budget of Earthquake Rupture With Coseismic Off-Fault Damage. J. Geophys. Res. Solid Earth 124, 11771–11801.

Okubo, K., Bhat, H.S., Rougier, E., Marty, S., Schubnel, A., Lei, Z., Knight, E.E., Klinger, Y., 2019. Dynamics, radiation, and overall energy budget of earthquake rupture with coseismic off-fault damage. J Geophys Res Solid Earth 11771–11801.

Pan, J., Li, H., Chevalier, M.-L., Tapponnier, P., Bai, M., Li, Chao, Liu, F., Liu, D., Wu, K., Wang, P., Li, Chunrui, Lu, H., Chen, P., 2022. Co-seismic rupture of the 2021, Mw7.4 Maduo earthquake (northern Tibet): Short-cutting of the Kunlun fault big bend. Earth Planet. Sci. Lett. 594, 117703. https://doi.org/10.1016/j.epsl.2022.117703

Passelègue, F.X., Pimienta, L., Faulkner, D., Schubnel, A., Fortin, J., Guéguen, Y., 2018. Development and Recovery of Stress-Induced Elastic Anisotropy During Cyclic Loading Experiment on Westerly Granite. Geophys. Res. Lett. 45, 8156–8166. https://doi.org/10.1029/2018GL078434

Perrin, C., Manighetti, I., Ampuero, J.-P., Cappa, F., Gaudemer, Y., 2016. Location of largest earthquake slip and fast rupture controlled by along-strike change in fault structural

maturity due to fault growth. J. Geophys. Res. Solid Earth 121, 3666–3685. https://doi.org/10.1002/2015JB012671

Perrin, C., Waldhauser, F., Scholz, C.H., 2021. The Shear Deformation Zone and the Smoothing of Faults With Displacement. J. Geophys. Res. Solid Earth 126, e2020JB020447. https://doi.org/10.1029/2020JB020447

Petersen, M., Dawson, T., Chen, R., Cao, T., Wills, C., Schwartz, D., Frankel, A., 2011. Fault Displacement Hazard for Strike-Slip Faults. Bull. Seismol. Soc. Am. - BULL Seism. SOC AMER 101, 805–825. https://doi.org/10.1785/0120100035

Qiu, H., Ben-Zion, Y., Catchings, R., Goldman, M.R., Allam, A.A., Steidl, J., 2021. Seismic Imaging of the Mw 7.1 Ridgecrest Earthquake Rupture Zone From Data Recorded by Dense Linear Arrays. J. Geophys. Res. Solid Earth 126, e2021JB022043. https://doi.org/10.1029/2021JB022043

Ren, J., Xu, X., Zhang, G., Wang, Q., Zhang, Z., Gai, H., Kang, W., 2022. Coseismic surface ruptures, slip distribution, and 3D seismogenic fault for the 2021 Mw 7.3 Maduo earthquake, central Tibetan Plateau, and its tectonic implications. Tectonophysics 827, 229275. https://doi.org/10.1016/j.tecto.2022.229275

Ren, J., Zhang, Z., Gai, H., Kang, W., 2021. Typical Riedel shear structures of the coseismic surface rupture zone produced by the 2021 Mw 7.3 Maduo earthquake, Qinghai, China, and the implications for seismic hazards in the block interior. Nat. Hazards Res. 1, 145–152. https://doi.org/10.1016/j.nhres.2021.10.001

Rockwell, T., Lindvall, S., Dawson, T., Langridge, R., Lettis, W., Klinger, Y., 2002. Lateral offsets on surveyed cultural features resulting from the 1999 Izmit and Düzce

890 earthquakes, Turkey. Bull Seism. Soc Am 92, 79–94.
891 https://doi.org/10.1785/0120000809
892 Rodriguez Padilla, A.M., Oskin, M.E., 2023. Displacement Hazard from Distributed Ruptures in
893 Strike-Slip Earthquakes. Bull. Seismol. Soc. Am. https://doi.org/10.1785/0120230044
894 Rodriguez Padilla, A.M., Oskin, M.E., Milliner, C.W.D., Plesch, A., 2022. Accrual of
895 widespread rock damage from the 2019 Ridgecrest earthquakes. Nat. Geosci. 15, 222–
896 226. https://doi.org/10.1038/s41561-021-00888-w
897 Rosu, A.-M., Pierrot-Deseilligny, M., Delorme, A., Binet, R., Klinger, Y., 2015. Measurement of
898 ground displacement from optical satellite image correlation using the free open-source
899 software MicMac. ISPRS J Photogramm Remote Sens High-Resolut. Earth Imaging
900 Geospatial Inf. 100, 48–59. https://doi.org/10.1016/j.isprsjprs.2014.03.002
901 Rupnik, E., Daakir, M., Pierrot Deseilligny, M., 2017. MicMac – a free, open-source solution for
902 photogrammetry. Open Geospatial Data Softw Stand 2, 14.
903 https://doi.org/10.1186/s40965-017-0027-2
904 Rupnik, E., Deseilligny, M.P., Delorme, A., Klinger, Y., 2016. Refined satellite image
905 orientation in the free open-source photogrammetric tools Apero/MicMac. ISPRS Ann
906 Photogramm Remote Sens 3, 83–90. https://doi.org/10.5194/isprsannals-III-1-83-2016
907 Sammis, C., Rosakis, A., Bhat, H., 2009. Effects of off-fault damage on earthquake rupture
908 propagation: Experimental studies, in: Ben-Zion, Y., Sammis, C. (Eds.), Mechanics,
909 Structure and Evolution of Fault Zones. Pageoph Topical Volumes, Birkhäuser Basel. pp.
910 1629–1648. https://doi.org/10.1007/978-3-0346-0138-2_5

911 Savage, H.M., Brodsky, E.E., 2011. Collateral damage: Evolution with displacement of fracture
912 distribution and secondary fault strands in fault damage zones. J. Geophys. Res. Solid
913 Earth 116. https://doi.org/10.1029/2010JB007665
914 Scholz, C.H., 1998. Earthquakes and friction laws. Nature 391, 37–42.
915 https://doi.org/10.1038/34097
916 Scott, C.P., Arrowsmith, J.R., Nissen, E., Lajoie, L., Maruyama, T., Chiba, T., 2018. The M7
917 2016 Kumamoto, Japan, Earthquake: 3-D Deformation Along the Fault and Within the
918 Damage Zone Constrained From Differential Lidar Topography. J. Geophys. Res. Solid
919 Earth 123, 6138–6155. https://doi.org/10.1029/2018JB015581
920 Segall, P., 2010. Earthquake and Volcano Deformation, STU-Student. ed. Princeton University
921 Press.
922 Simone, B., Andrenacci, C., Daniele, C., Scott, C., Brozzetti, F., Arrowsmith, R., Lavecchia, G.,
923 2022. High-Detail Fault Segmentation: Deep Insight into the Anatomy of the 1983 Borah
924 Peak Earthquake Rupture Zone (Mw 6.9, Idaho, USA). Lithosphere 2022.
925 https://doi.org/10.2113/2022/8100224
926 Teran, O.J., 2015. Geologic and structural controls on rupture zone fabric: A field-based study of
927 the 2010 Mw 7.2 El Mayor–Cucapah earthquake surface rupture. Geosphere 11, 899–
928 920.
929 Thomas, M.Y., Bhat, H.S., 2018. Dynamic evolution of off-fault medium during an earthquake:
930 a micromechanics based model. Geophys. J. Int. 214, 1267–1280.
931 https://doi.org/10.1093/gji/ggy129
932 Thompson, B.D., Young, R.P., Lockner, D.A., 2006. Fracture in Westerly Granite under AE
933 Feedback and Constant Strain Rate Loading: Nucleation, Quasi-static Propagation, and

the Transition to Unstable Fracture Propagation. Pure Appl. Geophys. 163, 995–1019. https://doi.org/10.1007/s00024-006-0054-x

Torabi, A., Johannessen, M., Ellingsen, T., 2019. Fault Core Thickness: Insights from Siliciclastic and Carbonate Rocks. Geofluids 2019, 1–24. https://doi.org/10.1155/2019/2918673

Vidale, J.E., Li, Y.-G., 2003. Damage to the shallow Landers fault from the nearby Hector Mine earthquake. Nature 421, 524–526. https://doi.org/10.1038/nature01354

Visage, S., Souloumiac, P., Cubas, N., Maillot, B., Antoine, S.L., Delorme, A., Klinger, Y., 2023. Evolution of the off-fault deformation of strike-slip faults in a sand-box experiment. Tectonophysics 847, 229704. https://doi.org/10.1016/j.tecto.2023.229704

Wang, W., Fang, L., Wu, J., Tu, H., Chen, L., Lai, G., Zhang, L., 2021. Aftershock sequence relocation of the 2021 MS7.4 Maduo Earthquake, Qinghai, China. Sci. China Earth Sci. 64, 1371–1380. https://doi.org/10.1007/s11430-021-9803-3

Wang, Y., Day, S.M., 2017. Seismic source spectral properties of crack-like and pulse-like modes of dynamic rupture. J. Geophys. Res. Solid Earth 122, 6657–6684. https://doi.org/10.1002/2017JB014454

Wei, S., Zeng, H., Shi, Q., Liu, J., Luo, H., Hu, W., Li, Y., Wang, W., Ma, Z., Liu-Zeng, J., Wang, T., 2022. Simultaneous Rupture Propagation Through Fault Bifurcation of the 2021 Mw7.4 Maduo Earthquake. Geophys. Res. Lett. 49, e2022GL100283. https://doi.org/10.1029/2022GL100283

Xie, H., Li, Z., Yuan, D., Wang, X., Su, Q., Li, X., Wang, A., Su, P., 2022. Characteristics of Co-Seismic Surface Rupture of the 2021 Maduo Mw 7.4 Earthquake and Its Tectonic

Implications for Northern Qinghai–Tibet Plateau. Remote Sens. 14, 4154. https://doi.org/10.3390/rs14174154

Xiong, W., Chen, W., Wang, D., Wen, Y., Nie, Z., Gang, L., Dijin, W., Yu, P., Qiao, X., Zhao, B., 2022. Coseismic slip and early afterslip of the 2021 Mw 7.4 Maduo, China earthquake constrained by GPS and InSAR data. Tectonophysics 840, 229558. https://doi.org/10.1016/j.tecto.2022.229558

Yamamoto, K., Sato, N., Yabe, Y., 2002. Elastic property of damaged zone inferred from in-situ stresses and its role on the shear strength of faults. Earth Planets Space 54, 1181–1194. https://doi.org/10.1186/BF03353319

Yang, H., 2015. Recent advances in imaging crustal fault zones: a review. Earthq. Sci. 28, 151–162. https://doi.org/10.1007/s11589-015-0114-3

Yang, H., Zhu, L., Cochran, E.S., 2011. Seismic structures of the Calico fault zone inferred from local earthquake travel time modelling. Geophys. J. Int. 186, 760–770. https://doi.org/10.1111/j.1365-246X.2011.05055.x

Yang, Y.-H., Xu, Q., Hu, J.-C., Wang, Y.-S., Dong, X.-J., Chen, Q., Zhang, Y.-J., Li, H.-L., 2022. Source Model and Triggered Aseismic Faulting of the 2021 Mw 7.3 Maduo Earthquake Revealed by the UAV-Lidar/Photogrammetry, InSAR, and Field Investigation. Remote Sens. 14, 5859. https://doi.org/10.3390/rs14225859

Yuan, J., Li, Y., 2023. Complex fault geometry controls dynamic rupture of the 2021 Mw7.4 Maduo earthquake, NE Tibetan Plateau. Tectonophysics 230105. https://doi.org/10.1016/j.tecto.2023.230105

Yuan, Z., Li, T., Su, P., Sun, H., Ha, G., Guo, P., Chen, G., Jobe, J., 2022. Large Surface-Rupture Gaps and Low Surface Fault Slip of the 2021 Mw 7.4 Maduo Earthquake Along

a Low-Activity Strike-Slip Fault, Tibetan Plateau. Geophys. Res. Lett. 49. https://doi.org/10.1029/2021GL096874

Yuan, Z., Liu-Zeng, J., Li, X., Xu, J., Yao, W., Han, L., Li, T., 2020. Detailed mapping of the surface rupture of the 12 February 2014 Yutian Ms7.3 earthquake, Altyn Tagh fault, Xinjiang, China. Sci. China Earth Sci. 64. https://doi.org/10.1007/s11430-020-9673-6

Yue, H., Shen, Z.-K., Zhao, Z., Wang, T., Cao, B., Li, Z., Bao, X., Zhao, L., Song, X., Ge, Z., Ren, C., Lu, W., Zhang, Y., Liu-Zeng, J., Wang, M., Huang, Q., Zhou, S., Xue, L., 2022. Rupture process of the 2021 M7.4 Maduo earthquake and implication for deformation mode of the Songpan-Ganzi terrane in Tibetan Plateau. Proc. Natl. Acad. Sci. 119, e2116445119. https://doi.org/10.1073/pnas.2116445119

Zhang, X., Feng, W., Du, H., Samsonov, S., Yi, L., 2022. Supershear Rupture During the 2021 MW 7.4 Maduo, China, Earthquake. Geophys. Res. Lett. 49, e2022GL097984. https://doi.org/10.1029/2022GL097984

Zhao, D., Qu, C., Bürgmann, R., Shan, X., 2023. Characterizing Deep, Shallow, and Surface Fault Zone Deformation of the 2021 Mw 7.4 Maduo, China, Earthquake. Seismol. Res. Lett. https://doi.org/10.1785/0220230115

Zhao, D., Qu, C., Chen, H., Shan, X., Song, X., Gong, W., 2021. Tectonic and Geometric Control on Fault Kinematics of the 2021 Mw7.3 Maduo (China) Earthquake Inferred From Interseismic, Coseismic, and Postseismic InSAR Observations. Geophys. Res. Lett. 48. https://doi.org/10.1029/2021GL095417

Zhao, L., Xu, W., Xie, L., Zhao, D., Zhu, Z., Wu, P., Guo, H., 2023. Fault geometry and low frictional control of the near-field postseismic deformation of the 2021 Mw 7.3 Maduo earthquake. Tectonophysics 863, 230000. https://doi.org/10.1016/j.tecto.2023.230000

1002 Zheng, A., Yu, X., Qian, J., Liu, X., Zhang, W., Chen, X., Xu, W., 2023. Cascading rupture
1003 process of the 2021 Maduo, China earthquake revealed by the joint inversion of seismic
1004 and geodetic data. Tectonophysics 849, 229732.
1005 https://doi.org/10.1016/j.tecto.2023.229732
1006 Zhou, Z., Bianco, M., Gerstoft, P., Olsen, K., 2022. High-Resolution Imaging of Complex
1007 Shallow Fault Zones Along the July 2019 Ridgecrest Ruptures. Geophys. Res. Lett. 49,
1008 e2021GL095024. https://doi.org/10.1029/2021GL095024
1009